A Flywheel Energy Storage System Demonstration for Space Applications

Barbara H. Kenny
National Aeronautics and Space Administration
Glenn Research Center
Cleveland, OH 44135

Peter E. Kascak, Ralph Jansen
University of Toledo
Toledo, OH 44444

Timothy Dever
QSS Group, Inc
Cleveland, OH 44135

Abstract- **A novel control algorithm for the charge and discharge modes of operation of a flywheel energy storage system for space applications is presented. The motor control portion of the algorithm uses sensorless field oriented control with position and speed estimates determined from a signal injection technique at low speeds and a back EMF technique at higher speeds. The charge and discharge portion of the algorithm use command feed-forward and disturbance decoupling, respectively, to achieve fast response with low gains. Simulation and experimental results are presented.**

I. INTRODUCTION

Presently, energy storage on the Space Station and satellites is accomplished using chemical batteries, most commonly nickel hydrogen or nickel cadmium. A flywheel energy storage system is an alternative technology that is being considered for future space missions. Flywheels offer the advantage of a longer lifetime, higher efficiency and a greater depth of discharge than batteries. However, several advanced technologies must be demonstrated for the flywheel energy storage system to be a viable option for future space missions. These include high strength composite materials, highly efficient high speed motor operation and control, and magnetic bearing levitation. To demonstrate the successful combination of these technologies, a flywheel energy storage system testbed has been constructed at the NASA Glenn Research Center.

The main components of the flywheel energy storage system are the composite rotor, motor/generator, magnetic bearings, touchdown bearings, and vacuum housing. The flywheel system is designed for 364 watt-hours of energy storage at 60,000 rpm and uses active magnetic bearings to provide a long-life, low-loss suspension of the rotating mass. The upper bearing of the unit is a combination magnetic bearing, providing suspension axially as well as radially. The lower magnetic bearing suspends the shaft in the radial direction only. At each end of the shaft there is also a touchdown bearing. This provides a back up bearing system should the magnetic bearings fail during testing.

The motor/generator unit is located at the lower end of the shaft. It consists of a two-pole rotor piece with surface mounted samarium cobalt magnets and a carbon fiber retaining wrap. On the stator side, there are three phase sinusoidally distributed windings in twelve slots. A water jacket around the stator provides cooling. Field orientation and a combination of mechanical sensorless techniques are used to control the motor from zero and low speed up to full speed operation [1]. The self-sensing technique [2] is used at zero and low speeds to start the machine, then the control is switched to a back-EMF based sensorless technique [3] for the normal higher speed operating range of the machine. This combined technique was previously demonstrated in [4] however the machine used in that case was an interior PM machine for an electric vehicle application.

The torque command to the field orientation algorithm is provided by an outer loop control algorithm that regulates the flywheel motor during both charge (motoring) and discharge (generating) operation [5,6]. During charge mode, the flywheel can be charged at a constant power rate with the appropriate torque command while during discharge, the flywheel provides the power necessary to regulate the DC bus to a set value.

The purpose of this paper is to present the experimental results demonstrating the transition between the charge and discharge modes of operation and the regulation of the DC bus during discharge operation under electrical load disturbances with magnetic bearing suspension and sensorless control of the motor/generator.

II. MOTOR/GENERATOR AND CONTROL

The rated power of the two pole surface mount PM machine is 1.5 kW and the rated phase voltage is 65 volts peak. At full speed, 60,000 rpm, the fundamental frequency is 1 kHz.

The block diagram of the controller is shown in Fig. 1. As stated previously, the inner loop torque control of the motor is based on the field orientation algorithm using one of two sensorless position estimates. The rotor reference frame q-axis current command is provided by the charge/discharge controller (described in the next section).

The control algorithm starts the motor using an initiation algorithm to set the rotor to a known position as described in [7]. Then the self-sensing algorithm [2] is used to accelerate the motor from standstill to 1200 rpm. The self-sensing technique requires a position dependent magnetic saliency in the machine. The flywheel motor has a small saliency as can be seen in the static phase to phase inductance measurement as a function of position as shown in Fig. 2.

At 1200 rpm, the control is transferred to the back-EMF method [3] and the carrier signal voltage necessary for the self-sensing method, $\mathbf{V}_{qds\_c}^{s*}$, is gradually removed. The estimated position from each of the methods is shown at this transition point in Fig. 3. The transition occurs at time t=0 with the system operating using the self-sensing technique for t<0 and with the back EMF technique for t>0. Both methods
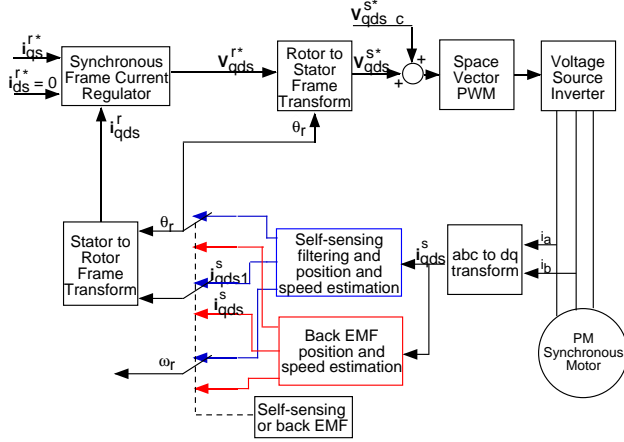
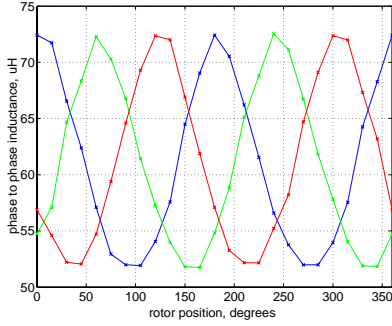Figure 1: Block diagram of flywheel motor control.

Figure 2: Measured phase to phase inductance variation with rotor position.

are producing reliable position and speed estimates at this point.

The machine does not have a resolver or encoder to verify the absolute accuracy of the position estimate. However, the machine does have a "once around" (OAR) signal that produces one pulse every mechanical revolution. The OAR signal can be used to estimate the position and speed as described in [8]. Fig. 3 shows the self-sensing position estimate from t=-.2 to 0, the back EMF position estimate from t=0 to .2, and the difference between each of the estimates and the OAR estimate. It can be seen that all three estimates agree to within 5 degrees.
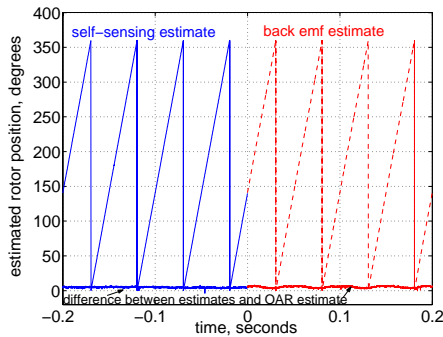

Figure 3: Estimated rotor position during self-sensing to back emf transition

For the purposes of this paper, it is sufficient to describe in more detail only the back-EMF estimation technique because the operation of interest is at the higher speeds. Further information on the combined technique can be found in [1,4].

A. Back-EMF estimation technique

The stator reference frame equation describing the relationship between the stator voltage, current and flux linkages for the fundamental excitation of the machine is given in (1).

$$\mathbf{v}_{qds}^{s} = \mathbf{i}_{qds}^{s} R_s + p\lambda_{qds}^{s} \tag{1}$$

The stator flux can be estimated by integrating the stator voltage less the IR drop as shown in (2).

$$\lambda_{qds}^{s} = \int \left(\mathbf{v}_{qds}^{s} - \mathbf{i}_{qds}^{s} R_s \right) dt \tag{2}$$

In the actual implementation, a low pass filter is used instead of pure integration. The torque angle, δ, can be found by expressing the stator flux in the rotor reference frame as shown in (3), (4) and (5).

$$\lambda_{qs}^{r} = L_q i_{qs}^{r} \tag{3}$$

$$\lambda_{ds}^{r} = L_d i_{ds}^{r} + \lambda_{af} \tag{4}$$

$$\delta = \tan^{-1}\left(\frac{L_q i_{qs}^{r}}{L_d i_{ds}^{r} + \lambda_{af}} \right) \tag{5}$$

The estimated rotor flux position angle, $\hat{\theta}_r$, is found from (6) and shown graphically in Fig. 4.

$$\hat{\theta}_r = \tan^{-1}\left(\frac{\lambda_{qs}^{s}}{\lambda_{ds}^{s}} \right) - \delta \tag{6}$$
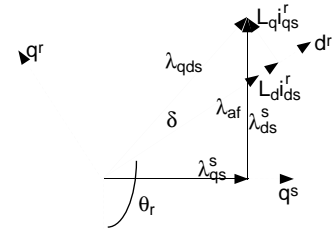

Figure 4: Vector diagram showing flux, current and angles

This angle estimate is then used in a Luenberger style observer, along with the estimated motor torque, to estimate the rotor speed as shown in Fig. 5 [9].
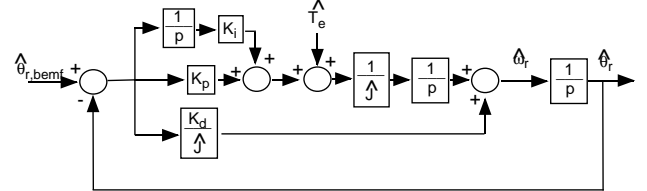

Figure 5: Speed observer

III. FLYWHEEL CONTROL

There are three modes of operation for the flywheel in a spacecraft power system: charge, charge reduction and discharge. In charge mode, the solar array produces enough current to charge the flywheel at its setpoint and to provide the required load current. The solar array electronics regulate the DC bus voltage during charge mode. In charge reduction mode, the solar array continues to provide load current but it can not provide enough current to charge the flywheel at its setpoint. When this occurs, the DC bus voltage regulation function is transferred to the flywheel system. Finally, in discharge mode, the flywheel system provides all the load current and regulates the DC bus voltage. The features of each mode are given in Table 1 and the corresponding block diagram is shown in Fig. 6.

Table 1: Flywheel system operating mode characteristics

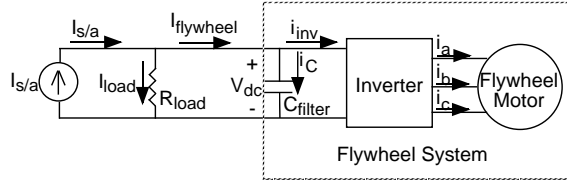| Mode	Current	DC Bus Voltage
Full Sun "Charge"	$I_{s/a} = I_{load} + I^*_{charge}$ $I_{flywheel} = I^*_{charge}$	Regulated by solar array system
Partial Sun "Charge Reduction"	$I_{load} + I^*_{charge} > I_{s/a} > 0$ $I_{flywheel} < I^*_{charge}$	Regulated by flywheel system
Eclipse "Discharge"	$I_{load} = -I_{flywheel}$ $I_{flywheel} < 0$	Regulated by flywheel system

Figure 6: Basic block diagram model of spacecraft power distribution system with flywheel energy storage.

The motor is operated using field oriented control with the rotor reference frame d-axis current command set equal to zero and q-axis current command derived from the flywheel current requirements shown in Table 1. The motor currents are regulated to the commanded values using a synchronous frame PI regulator as shown in Fig. 1.

The relationship between the flywheel current and the motor current is based on a steady state power balance between the DC power going into the inverter and the AC power going to the motor. This is shown in (7) where inverter losses are neglected and $\overline{i_{inv}}$ is the average DC current into the inverter and is equal to $I_{flywheel}$ under steady state conditions.

$$\overline{i_{inv}}\, V_{dc} = \frac{3}{2}(v^r_{qs}i^r_{qs} + v^r_{ds}i^r_{ds}) \tag{7}$$

The q-axis voltage, v^r_{qs}, can be expressed as shown in (8) [10].

$$v^r_{qs} = i^r_{qs}R_s + L_{qs}pi^r_{qs} + i^r_{ds}\omega_r L_{ds} + \omega_r\lambda_{af} \tag{8}$$

Noting that i^r_{ds} is regulated to zero, neglecting the derivative term due to the assumption of steady state conditions, and combining (7) and (8) gives the following result.

$$\overline{i_{inv}}\, V_{dc} = \frac{3}{2}((i^r_{qs}R_s + \omega_r\lambda_{af})i^r_{qs}) \tag{9}$$

The voltage drop across the stator resistor, $i^r_{qs}R_s$, is small compared to the back EMF voltage, $\omega_r\lambda_{af}$, especially at the high speeds used for the flywheel system. Neglecting $i^r_{qs}R_s$ and rearranging results in the approximate relationship between the motor current and the DC side current as shown.

$$i^r_{qs} \approx \overline{i_{inv}}\,\frac{2\,V_{dc}}{3\omega_r\lambda_{af}} \tag{10}$$

This relationship between the motor current and the average inverter current becomes the basis for controlling the flywheel motor in all modes of operation defined by Table 1. In charge mode, it is used as a feed-forward term in the controller and in charge reduction and discharge modes (when the flywheel system is regulating the DC voltage) it is used as a disturbance decoupling term.

IV. CHARGE, CHARGE REDUCTION AND DISCHARGE CONTROL

In charge mode, the flywheel charges at a constant power, constant DC current rate using the excess current from the solar array. The charge control algorithm regulates the acceleration of the flywheel motor so that the DC current is maintained at the commanded set point. The block diagram of the charge control algorithm is shown in Fig. 7.

There are two components to the controller: the proportional-integral (PI) and the feed-forward (FF). The feed-forward portion uses the DC charging current command and converts it into a motor current command using the relationship given in (10), the measured DC bus voltage and the estimated rotor speed from the back EMF estimation algorithm. The PI portion makes up for any inaccuracies in the relationship given in (10) and guarantees zero steady state error. Thus fast, accurate performance is achieved with relatively low gains.

In charge reduction and discharge modes, the flywheel motor must decelerate at the appropriate rate to maintain the DC bus voltage at the commanded value while supplying the
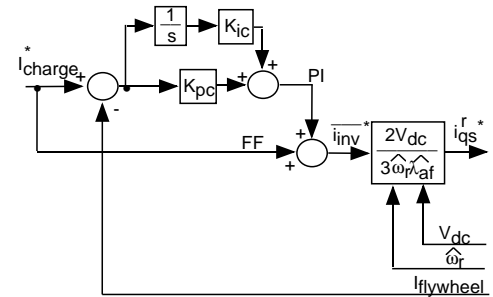

Figure 7: Charge control block diagram.

necessary current to the loads. The block diagram for this algorithm is shown in Fig. 8.

Again, there are two components to the controller: the PI portion and a disturbance decoupling portion (DD). In the decoupling portion, the DC flywheel current is measured and used as an early indicator to the controller whether there has been an increase or decrease in load. If there is a sudden increase in load, the capacitor will initially maintain the bus voltage and there will be an increase in the DC current, $I_{flywheel}$, to supply the new load. This increase in $I_{flywheel}$ is measured and used to calculate the corresponding motor current. Thus the motor responds by decelerating more quickly, even before a drop in the DC bus voltage causes the PI portion to respond.

In the PI portion the measured DC bus voltage is compared to the commanded DC bus voltage and the error signal is inverted. This is because (using the direction references of Fig. 6) the average inverter current needs to become more negative for a decreasing DC bus voltage and less negative for an increasing one. The PI portion makes up for any inaccuracies in the disturbance decoupling portion and maintains the DC bus voltage at the set point.

The two controllers shown in Figs. 7 and 8 are combined to form the overall Charge/Discharge Current/Voltage Regulator (CDCVR) controller shown in Fig. 9. The system is in charge mode (current regulation) when the solar array provides enough current to meet both the load demands and the charging current to the flywheel system. Otherwise, the system is in charge reduction or discharge mode which means the flywheel system is regulating the DC voltage bus.

The transition from current regulation (Fig. 7) to voltage regulation (Fig. 8) is accomplished in the following manner. The solar array regulates the bus voltage to a set point value higher than the flywheel regulation set point as long as the solar array current is sufficient to provide both the load and the charging current, I^*_{charge}. Once the solar array current begins to drop off, the DC bus voltage begins to fall and the flywheel current, $I_{flywheel}$, also drops. This transition is detected in the controller by comparing the difference between the actual DC bus voltage and the flywheel set point voltage to the "voltage transition constant", VTC, as seen in Fig. 9. Once this difference is less than the VTC, the integrator in the PI portion of the controller is reset. This reduces the i^*_{inv} command at point 2 to a value slightly larger than $I_{flywheel}$. This value is then compared to the charge current set point, I^*_{charge}. If it is less than I^*_{charge}, which it will
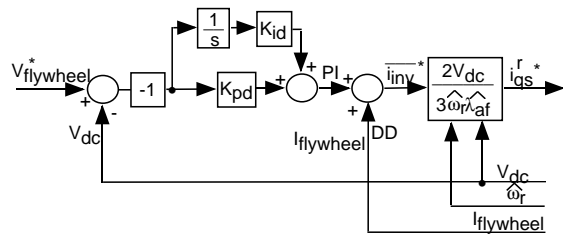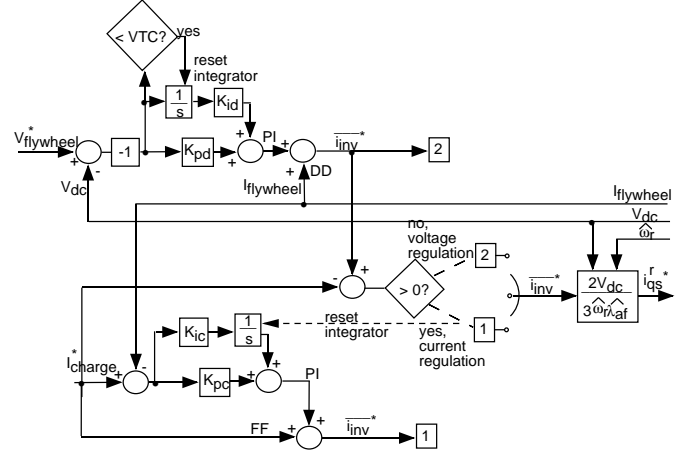

Figure 9: CDCVR control block diagram.

be if the solar array is not producing enough current, then the system transitions into charge reduction mode where the DC bus voltage is regulated by the flywheel system.

Similarly, as the system moves from eclipse into sunlight, the solar array will produce more current. When the array produces enough current to meet the load demand, the i^*_{inv} command at point 2 in the controller will become positive. When it exceeds the charge current set point, I^*_{charge}, the integrator in the current regulator portion of the controller is reset and the system transitions back into charge mode where the flywheel system regulates the current into the flywheel and the solar array system regulates the DC bus voltage.

The three modes of operation: charge, charge reduction and discharge, were defined based on a battery energy storage system. Because the flywheel system is intended to replace batteries, these modes were duplicated in the flywheel system control. However, the flywheel energy storage system is capable of regulating the DC bus voltage both when charging and discharging, obviating the need for multiple modes and the transition between them. Designing the flywheel system control to perform this regulation at all times would result in an overall simpler control strategy, even when considering the necessary provisions to prevent over-speed or over-current operation. This is an area for future study.

V. SIMULATION RESULTS

The performance of the CDCVR controller was simulated using a model that included all of the blocks of Figs. 1 and 9 except the inverter (PWM switching was neglected) and the self-sensing portion (which is only used for start-up). The spacecraft bus was modeled as a capacitance in parallel with a resistive load (Fig. 6), similar to the experimental set up, and the solar array was modeled as a voltage-regulated current source. In charge mode, the DC bus voltage set point is 125 volts and in discharge mode, the set point is 120 volts. These values are representative of a future spacecraft system. There is 4800 μF of capacitance on the DC bus.

Figures 10-13 show the simulation results. The system is initially in the charge mode at 50,000 rpm and charging at a

Figure 8: Discharge and charge reduction control block diagram.

constant current of 1.5 amps. At time t=3 seconds, the available current from the source is reduced and the DC bus voltage begins to drop. The system goes into charge reduction mode and the flywheel begins to regulate the DC bus voltage to 120 volts. From time t=3 to t=3.5, the source is still providing enough current to meet the load and to charge the flywheel system, although at a slower and slower rate. At time t=3.5, the source no longer provides enough additional current to charge the flywheel and at t=4, the source current goes to zero and the flywheel system provides all of the current for the load. At t=7, a step change in load occurs. It can be seen that no transient occurs on the DC bus voltage. This is due to the action of the disturbance decoupling portion of the controller as shown in Fig. 8. The controller uses the measured flywheel current to increase the motor current command as soon as the load is added, before the bus voltage drops. Finally, at t=9, the available current from the source is increased and the system moves from discharge back into charge mode.

VI. EXPERIMENTAL RESULTS

The experimental set-up was similar to the block diagram shown in Fig. 6. The "solar array" was a DC power supply with current limiting capability, set to regulate the bus to 125 volts. The "load resistor" consisted of two parallel resistors, 300Ω and 200Ω. The resistors were connected such that two R_{load} values were available: 300Ω or 120Ω. The current was measured at the three points corresponding to $I_{s/a}$, $I_{flywheel}$ and I_{load} in Fig. 6. The control algorithm was written in Simulink[1] and executed using a dSpace[1] digital controller. The dSpace[1] data acquisition system was used to capture the data and Matlab[1] was used to create the plots.

The flywheel speed was limited to 11,000 rpm or less for these tests because the magnetic bearings for the system had not yet been optimally tuned for higher speed operation. This speed limit also limited the amount of power that the flywheel system could provide during discharge and continue to maintain the DC bus voltage. Two sets of data are shown in the following plots. Figures 14-17 show the results for a charge to charge reduction to discharge mode change followed by a step change in load. Figures 18-21 show a step change in load while in discharge mode followed by a mode change to charge mode operation.

In the first set of data, the current limit on the DC power supply is reduced at time t=0 and the bus voltage begins to fall. The CDCVR controller changes from charge mode operation (Fig. 7) to charge reduction/discharge operation (Fig. 8) and regulates the bus voltage to 120 volts. From t=0 to t=2, the system is in charge reduction mode as the power supply continues to provide current to the load. After t=2, the
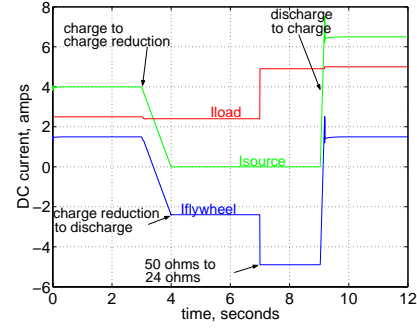
Figure 10: Simulation results of DC currents during mode transitions and step change in load
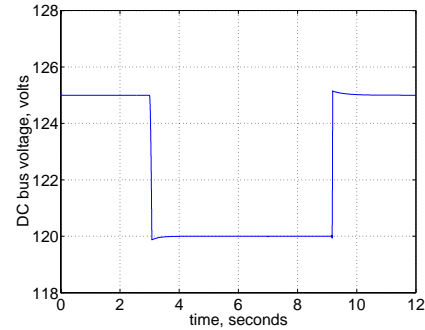

Figure 11: Simulation results of DC bus voltage during mode transitions and step change in load.
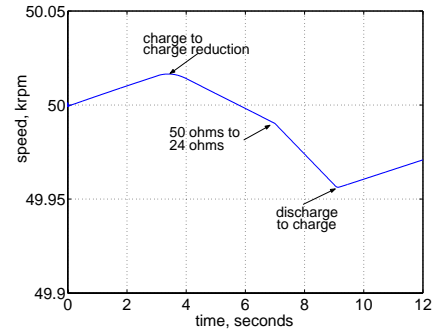

Figure 12: Simulation results of flywheel rotor speed during mode transitions and step change in load.
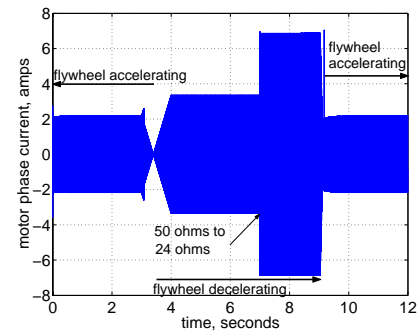

Figure 13: Simulation results of motor phase currents during mode transitions and step change in load.

flywheel system is supplying all of the current to the load and at approximately t=4.5 the parallel 200Ω load is added. The DC bus voltage exhibits a slight decrease, less than a volt, during the transition. It should be noted that the disturbance

decoupling is not as accurate at low speeds as at higher speeds. This can be seen from (10) where the stator resistance has been neglected to form the relationship between the average inverter current and the motor current.
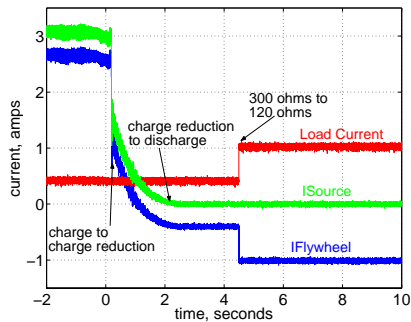

Figure 14: DC current during charge to discharge operation with a step change in load.
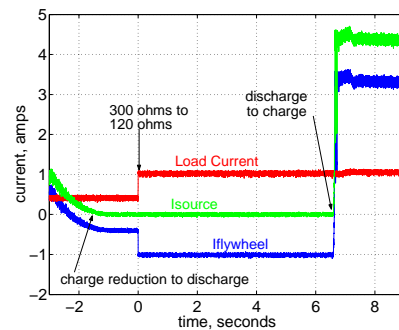

Figure 18: DC current for a step change in load and a discharge to charge mode transition.
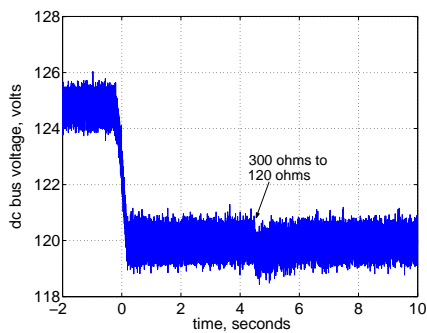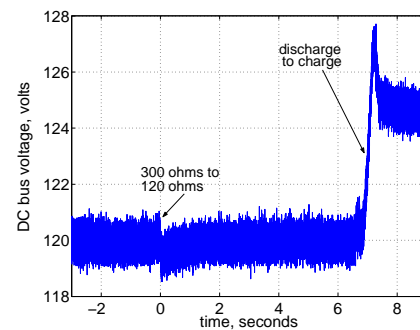

Figure 15: DC bus voltage.

Figure 19: DC bus voltage.
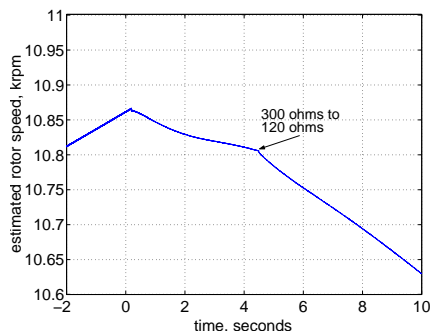

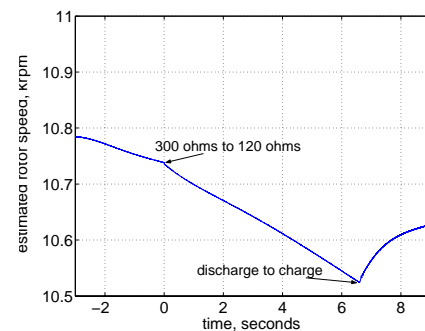Figure 16: Estimated rotor speed.

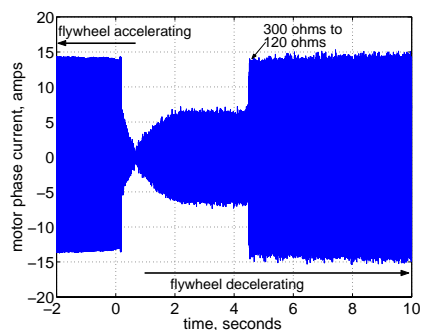Figure 20: Estimated rotor speed.

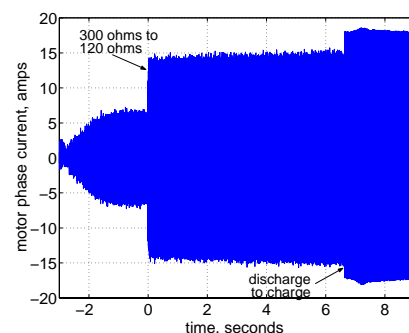
Figure 17: Motor phase current.

Figure 21: Motor phase current.

At lower speeds, neglecting this resistance causes more error in the approximation.

Fig. 16 shows the estimated rotor speed during the transitions. It is interesting to note that the flywheel current is still positive for .8 seconds past where the speed is starting to decrease. Ideally, as shown in simulation, the speed begins to decrease at the same time as the flywheel current becomes negative. The difference observed experimentally is due to losses in the system. Although the flywheel current is positive, not all of it is available to accelerate the motor due to losses in the inverter. This can also be seen from the motor current as shown in Fig. 17. The motor current envelope transitions through zero as the rotor moves from accelerating to decelerating as seen in simulation (Fig. 13). However, experimentally the speed is decreasing slightly prior to the motor current transition. This represents losses on the ac side of the inverter: filter and motor losses.

The second set of data shows three transitions as seen in the DC currents in Fig. 18. The system starts in charge reduction mode, then moves into discharge mode when the source current goes to zero. In both modes the flywheel system is regulating the DC bus voltage to 120 volts. Then the parallel 200Ω load is added at t=0. A slight dip in voltage is again observed in Fig. 19 as the load is increased. Fig. 20 shows the speed of the rotor decreasing more rapidly with the additional load, as expected. Fig. 21 shows the motor current increasing to handle the additional load.

At approximately t=7 the DC power supply current limit is stepped from zero to 10 amps. The power supply can now source enough current to meet the load demand and charge the flywheel at 3 amps. The system transitions into charge mode and the voltage is regulated by the power supply to 125 volts. The voltage transition is determined by the characteristics of the power supply, not the CDCVR control, and it overshoots slightly before settling at 125 volts. The speed increases at the transition and, although difficult to see from Fig. 21, the motor current envelope moves through zero as the motor changes from decelerating to accelerating.

It is interesting to note the speed estimates given in Figs. 16 and 20. The speed estimate is derived from the observer as described earlier and shown in Fig. 5. The response of the speed observer to sudden changes in the estimated position, resulting from sudden changes in the commanded voltage, depends on the gains. In Fig. 20 especially, it is apparent that the speed observer is responding to the disturbance resulting from the discharge to charge mode transition. It is most likely that the speed is not actually increasing on the arc shown but rather on a straight line to which the arc converges. Work is continuing to refine the gains to the most appropriate values and additional data will be taken in the future using the once around signal (OAR) estimate for calibration.

VII. CONCLUSIONS AND FUTURE WORK

This paper has presented a new algorithm for regulating the charge and discharge modes of a flywheel energy storage system using a sensorless field orientation control algorithm to provide the inner loop torque control. The algorithm mimics the operational modes presently found in battery systems and would allow the flywheel system to replace batteries on future spacecraft. Experimental and simulation results show the successful control of the flywheel system permanent magnet motor in all modes of operation. Additionally, transition between modes and DC bus voltage regulation during step changes in load was also demonstrated.

A future application of flywheel technology is to use flywheels to combine the energy storage and the attitude control functions on a spacecraft. A minimum of four flywheels would be needed to provide three axes of attitude control plus power during eclipse. This is the direction of the future research at the NASA Glenn Research Center.

REFERENCES

[1]   B. H. Kenny, P. E. Kascak, "Sensorless Control of Permanent Magnet Machine for NASA Flywheel Technology Development", *37th Annual IECEC*, Washington DC., July 28-August 2, 2002. NASA TM 2002-211726.

[2]   P. Jansen and R. D. Lorenz, "Transducerless Position and Velocity Estimation in Induction and Salient AC Machines", *IEEE Transactions on Industry Applications*, Vol. 31, No. 2, March/April 1995 pp. 240-247.

[3]   R. Wu, and G. Slemon, "A Permanent Magnet Motor Drive Without a Shaft Sensor", *IEEE Transactions on Industry Applications*, Vol. 27, No. 5, September/October 1991, pp. 1005-1011.

[4]   N. Patel,, T. O'Meara, J. Nagashima, R. Lorenz, "Encoderless IPM Traction Drive for EV/HEV's", *Conference Record of the 2001 IEEE Industry Applications Conference*, Chicago, Il, October, 2001.

[5]   P.E. Kascak, B. H. Kenny, T. P. Dever, W. Santiago, R. H. Jansen, "International Space Station Bus Regulation with NASA Glenn Research Center Flywheel Energy Storage System Development Unit", *36th Annual IECEC*, Savannah, Ga., July 29-August 2, 2001. NASA TM 2001-211138.

[6]   B. H. Kenny, P. E. Kascak, "DC Bus Regulation with a Flywheel Energy Storage System", *Proceedings of the Society of Automotive Engineers Power Systems Conference*, October 29-31, 2002, Coral Springs, Fl., CD ROM. NASA TM 2002-211897.

[7]   N. Matsui, "Sensorless PM Brushless DC Motor Drives", *IEEE Transactions on Industrial Electronics*, Vol. 43, No. 2, April, 1996, pp. 300-308.

[8]   B. H. Kenny, et. al., "Advanced motor control test facility for NASA GRC flywheel energy storage system development unit", *Proceedings 36th Intersociety Energy Conversion Engineering Conference*, July 29-Aug. 2, 2001, CD ROM. NASA TM 2001-210986.

[9]   R. D. Lorenz, K.W. Van Patten, "High-resolution velocity estimation for all-digital, AC servo drives" *IEEE Transactions on Industry Applications*, Vol 27, No. 4, July/August 1991, pp. 701-705.

[10] R. Krishnan, *Permanent magnet synchronous and brushless DC motor drives: theory, operation, performance, modeling, simulation, analysis and design*, Virginia Polytechnical Institute, Blacksburg, Va., 1999.